Journal of Materials Chemistry A

PAPER

View Article Online
View Journal | View Issue

Thermoelectric properties of the $Yb_9Mn_{4.2-x}Zn_xSb_9$ solid solutions†

Cite this: *J. Mater. Chem. A*, 2014, **2**, 7478

Saneyuki Ohno,*[a] Alexandra Zevalkink,[ac] Yoshiki Takagiwa,[b] Sabah K. Bux[c] and G. Jeffrey Snyder[a]

Received 30th January 2014
Accepted 7th March 2014

DOI: 10.1039/c4ta00539b

www.rsc.org/MaterialsA

$Yb_9Mn_{4.2}Sb_9$ has been shown to have extremely low thermal conductivity and a high thermoelectric figure of merit attributed to its complex crystal structure and disordered interstitial sites. Motivated by previous work which shows that isoelectronic substitution of Mn by Zn leads to higher mobility by reducing spin disorder scattering, this study investigates the thermoelectric properties of the solid solution, $Yb_9Mn_{4.2-x}Zn_xSb_9$ (x = 0, 1, 2, 3 and 4.2). Measurements of the Hall mobility at high temperatures (up to 1000 K) show that the mobility can be increased by more than a factor of 3 by substituting Zn into Mn sites. This increase is explained by the reduction of the valence band effective mass with increasing Zn, leading to a slightly improved thermoelectric quality factor relative to $Yb_9Mn_{4.2}Sb_9$. However, increasing the Zn-content also increases the p-type carrier concentration, leading to metallic behavior with low Seebeck coefficients and high electrical conductivity. Varying the filling of the interstitial site in $Yb_9Zn_{4+y}Sb_9$ (y = 0.2, 0.3, 0.4 and 0.5) was attempted, but the carrier concentration ($\sim 10^{21}$ cm^{-3} at 300 K) and Seebeck coefficients remained constant, suggesting that the phase width of $Yb_9Zn_{4+y}Sb_9$ is quite narrow.

Introduction

Solid-state thermoelectric generators are an ideal clean and reliable source of an energy harvesting system due to their ability to generate electricity directly from waste heat. For the purpose of widespread applications, it is necessary to improve the efficiency of thermoelectric materials, quantified by the thermoelectric figure of merit ($zT = \alpha^2 T/\kappa\rho$).[1] A good thermoelectric material must strike a balance between a large Seebeck coefficient (α), low electrical resistivity (ρ), and low total thermal conductivity (κ), all of which are related *via* the free majority carrier concentration (n).[2] Here, the total thermal conductivity is a combination of electronic thermal conductivity (κ_{el}) and lattice thermal conductivity (κ_L).

Zintl compounds provide many of the characteristics required for good thermoelectric materials.[3,4] Zintl phases are made up of electropositive cations that donate their electrons to anions, which in turn must form covalent bonds to satisfy valence.[5,6] They often have very low lattice thermal conductivity due to their large unit cells, and it is possible to finely tune their electronic properties by doping, providing a route to improved zT. High thermoelectric efficiency has been demonstrated in a number of different Zintl compounds[7–17] including $Yb_{14}MnSb_{11}$ (ref. 16 and 18) and $YbCd_{2-x}Zn_xSb_2$, both of which have zT values above unity at high temperatures.[11,19–36]

Recently, $Yb_9Mn_{4.2}Sb_9$ was shown to have promising thermoelectric performance (zT = 0.7 at 950 K) by Bux *et al.*[17] The structure of $Yb_9M_{4+x}Sb_9$ is shown in Fig. 1, where M can be

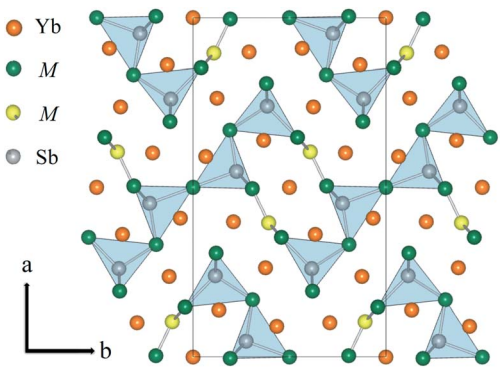

Fig. 1 The $Yb_9M_{4+x}Sb_9$ structure contains infinite M_4Sb_9 "ribbons" made up of corner sharing MSb_4 tetrahedra, where M is a 2+ transition metal that can be either Mn, Cd or Zn.[37,38] Partially occupied M-interstitial sites (yellow spheres) link neighboring M_4Sb_9 ribbons into a pseudo two-dimensional framework.

[a]*Materials Science, California Institute of Technology, 1200 E. California Blvd., Pasadena, CA 91125, USA. E-mail: sohno@caltech.edu*

[b]*Department of Advanced Materials Science, The University of Tokyo, Kiban-toh 502, 5-1-5 Kashiwanoha, Kashiwa-shi, Chiba 277-8561, Japan*

[c]*Thermal Energy Conversion Technologies Group, Jet Propulsion Laboratory, California Institute of Technology, 4800 Oak Grove Drive, MS 277-207, Pasadena, CA 91109, USA*

† Electronic supplementary information (ESI) available. See DOI: 10.1039/c4ta00539b

either Mn^{2+}, Cd^{2+} or Zn^{2+}.[37,38] Although this structure type was originally discovered in the 1970's,[39] the interstitial site was not recognized until 2004 by Bobev *et al.*[38] The structure contains ribbons of MSb_4 tetrahedra that are connected by partially occupied interstitial M sites. The $Yb_9M_{4+x}Sb_9$ structure would be charge balanced based on simple electron counting rules if the interstitial M sites were 25% occupied, corresponding to $x = 0.5$. In practice, the Mn analogue, $Yb_9Mn_{4+x}Sb_9$, was found to behave as a line compound with approximately 10% occupation of the interstitial sites ($x = 0.2$).[17,37] In the Zn-containing analogue, the exact composition is unclear, as the literature reports four different stoichiometries ($Yb_9Zn_{4.18}Sb_9$, $Yb_9Zn_{4.23}Sb_9$, $Yb_9Zn_{4.380}Sb_9$ and $Yb_9Zn_{4.384}Sb_9$) determined from refinement of single crystal X-ray diffraction data.[37,38]

The high zT reported for $Yb_9Mn_{4.2}Sb_9$ stems from its low, glass-like lattice thermal conductivity ($\kappa_L \simeq 0.5$ W mK^{-1} at room temperature) and optimized electronic properties.[17] To improve zT further, it is thus necessary to improve the inherent electronic properties of this system by tuning either the band structure or carrier scattering. One potential route is to increase the carrier mobility by substituting Zn on the Mn site, as demonstrated in the $YbZn_{2-x}Mn_xSb_2$ and $Yb_{14}Mn_{1-x}Zn_xSb_9$ solid solutions.[7,13] In $YbZn_{2-x}Mn_xSb_2$, the mobility of the Zn end-member is much higher than that of the Mn end-member, even though the effective mass remains unchanged. Similarly, in $Yb_{14}Mn_{1-x}Zn_xSb_{11}$, an increased Zn content leads to improved mobility. In both cases, the substitution of Zn leads to improved thermoelectric performance. These results motivate the current investigation of the thermoelectric properties of the $Yb_9Mn_{4.2-x}Zn_xSb_9$ solid solution ($x = 0$, 1, 2, 3 and 4.2).

Results and discussion

Synthesis and characterization

$Yb_9Mn_{4.2-x}Zn_xSb_9$ ($x = 0$, 1, 2, 3 and 4.2) and $Yb_9Zn_{4+y}Sb_9$ ($y = 2$, 3, 4 and 5) samples were prepared by ball milling followed by hot pressing (details are described in the Experimental section). To characterize these samples, X-ray diffraction (XRD) was performed on the polycrystalline slices at room temperature. Fig. 2 shows the XRD results for all of the $Yb_9Mn_{4.2-x}Zn_xSb_9$ samples ($x = 0$, 1, 2, 3 and 4.2). For the $x = 4.2$ sample, the Rietveld fit and residual are shown as red curves and blue curves respectively. Table 1 shows lattice parameters for solid solutions. As the amount of Zn increases, each lattice parameter varies linearly, in agreement with previously reported results.[37,38] Scanning electron microscopy confirmed that the phase purity of the Zn-containing samples is approximately 95% and revealed YbM_2Sb_2 (M = Zn or Mn) as a secondary phase.

Table 1 Lattice parameters for $Yb_9Mn_{4.2-x}Zn_xSb_9$ were calculated from XRD results using Rietveld fits. As the amount of Zn increases, each parameter changes linearly from the Mn end member side to the Zn end member and this follows a reported trend[37,38]

Composition	a (Å)	b (Å)	c (Å)
$x = 0$	22.014	12.231	4.6079
$x = 1$	21.834	12.327	4.5841
$x = 2$	21.764	12.334	4.5664
$x = 3$	21.711	12.343	4.5451
$x = 4.2$	21.692	12.409	4.5278

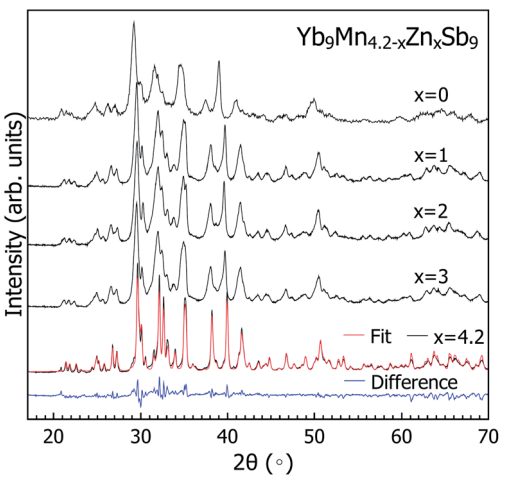

Fig. 2 X-ray diffraction patterns for $Yb_9Mn_{4.2-x}Zn_xSb_9$ ($x = 0$, 1, 2, 3 and 4.2) samples exhibit no significant impurity phases. The Rietveld fit and difference profiles are shown for the Zn end-member.

Electronic transport properties

The electronic transport properties of $Yb_9Mn_{4.2-x}Zn_xSb_9$ ($x = 0$, 1, 2, 3 and 4.2) samples are shown in Fig. 3 and 4. The Mn analogue, $Yb_9Mn_{4.2}Sb_9$, is a line compound with an electron deficient composition, resulting in a carrier concentration of

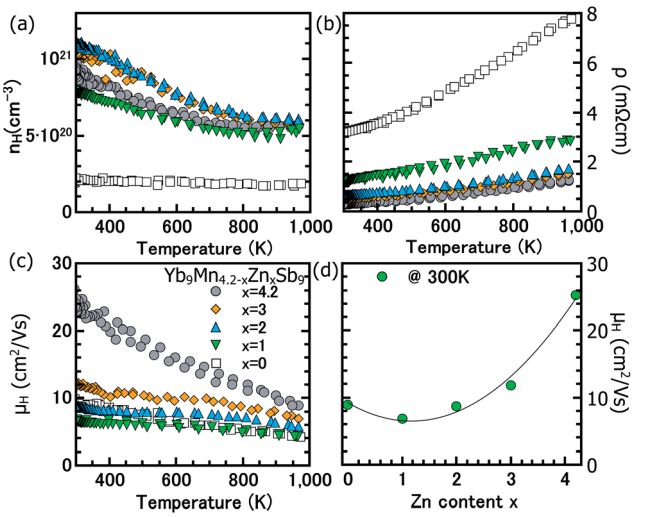

Fig. 3 With increasing Zn content, x, the (a) Hall carrier concentration of $Yb_9Mn_{4.2-x}Zn_xSb_9$ samples increases and (b) the resistivity decreases. (c) The Hall mobility decreases with temperature due to acoustic phonon scattering. (d) As a function of x at 300 K, the mobility decreases due to alloy scattering and then rises sharply with complete substitution of Mn by Zn.

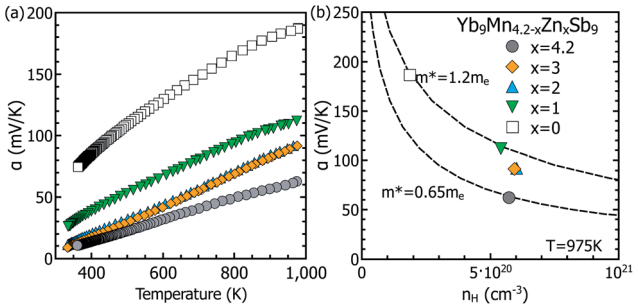

Fig. 4 (a) The Seebeck coefficients of $Yb_9Mn_{4.2-x}Zn_xSb_9$ ($x = 0$, 1, 2, 3 and 4.2) samples are consistent with degenerate semiconducting behavior. (b) The dashed curves, calculated with an SPB model using the parameters shown in Table 4, indicate that m^* decreases as the amount of Zn increases.

4×10^{20} h^+ cm^{-3} and degenerate semiconducting behavior. Surprisingly, considering that Zn and Mn both have the same valence state in this structure, substituting Zn on the Mn site increases the carrier concentration (n_H) sharply, as shown in Fig. 3a. Using simple electron counting rules, a carrier concentration of $n_H = 0$ h^+ cm^{-3} corresponds to 25% occupation of the interstitial sites ($Yb_9M_{4.5}Sb_9$), while completely empty interstitial sites ($Yb_9M_{4.0}Sb_9$) yield $n_H = 1.66 \times 10^{21}$ h^+ cm^{-3}. Thus, the higher n_H in Zn-containing samples may indicate that the solubility of Zn in the interstitial sites is lower than that of Mn. Additionally, in the Zn containing samples, n_H decreases by nearly an order of magnitude as the temperature increases. Both of these effects may be because introducing Zn changes the defect chemistry by lowering the energy to form accepter defects.[35]

The Hall mobility (μ_H) of $Yb_9Mn_{4.2-x}Zn_xSb_9$ samples (Fig. 3c) decreases with temperature as expected when acoustic phonons are the primary scattering source. The change in μ_H as a function of the Zn content at 300 K is shown in Fig. 3d. The mobility of the Zn end-member is increased by a factor of three relative to the Mn analogue. The slight reduction at intermediate values of x is due to the disorder on the transition metal site.[40]

An increase in mobility can arise from either increased carrier relaxation time (τ) or decreased effective mass (m^*). When acoustic phonon scattering controls the mobility, the scattering rate $1/\tau(k)$ is determined by the acoustic deformation potential (Ξ), acoustic phonon velocity (v_s), density (ρ), and the density of states ($g(E)$).[41]

$$\frac{1}{\tau(k)} = \frac{k_B T \Xi^2 \pi}{\hbar} \frac{g(E)}{v_s^2 \rho} \quad (1)$$

Substituting the density of states in three dimensions $\left(g_{3D}(E) = \frac{1}{2\pi^2}\left(\frac{2m^*}{\hbar^2}\right)^{3/2}\sqrt{E}\right)$ into eqn (1), yields the following relationship which shows that τ is also dependent on effective mass in this case.

$$\tau \propto \frac{1}{(m^*)^{3/2}}. \quad (2)$$

Inserting eqn (2) into the expression for mobility, the following proportionality is acquired for mobility limited by acoustic phonon scattering.

$$\mu \propto \frac{\tau}{m^*} \propto \frac{1}{(m^*)^{5/2}}. \quad (3)$$

The Seebeck coefficients (α) of $Yb_9Mn_{4.2-x}Zn_xSb_9$ ($x = 0$, 1, 2, 3 and 4.2) samples are shown as a function of temperature and carrier concentration in Fig. 4a and b, respectively. The Seebeck coefficients decrease as the amount of Zn, and thus the carrier concentration, increases. However the decrease in α is much greater than should be expected if m^* is unchanged. From the experimental Seebeck coefficients, the chemical potential (η) at 975 K is calculated within a single parabolic band (SPB)[10] model using eqn (4) with $\lambda = 0$ (acoustic-phonon scattering), where $F_j(\eta)$ is the Fermi integral given in eqn (6). The hole effective masses for the pure Zn and pure Mn samples (0.65 m_e and 1.2 m_e, respectively), determined from eqn (5) using the experimental n_H, were used to generate the dashed curves shown in Fig. 4b.

$$\alpha = \frac{k}{e}\left(\frac{(2+\lambda)F_{1+\lambda}(\eta)}{(1+\lambda)F_\lambda(\eta)} - \eta\right) \quad (4)$$

$$n = 4\pi\left(\frac{2m^*kT}{h^2}\right)^{3/2} F_{1/2}(\eta) \quad (5)$$

$$F_j(\eta) = \int_0^\infty \frac{\zeta^j d\zeta}{1 + \exp[\zeta - \eta]} \quad (6)$$

From eqn (3), we can see that the observed difference in m^* can fully explain the difference in mobility between the Mn and Zn analogues of the $Yb_9M_{4.2}Sb_9$ structure. An increased τ due to reduced spin disorder scattering is thus not necessary to explain the increased mobility in this case. This is in contrast to the $YbZn_{2-x}Mn_xSb_2$ system, in which m^* remained constant, and τ increased upon Zn substitution.

Thermal transport properties

As shown in Fig. 5a, the total thermal conductivity (κ_{total}) for $Yb_9Mn_{4.2-x}Zn_xSb_9$ samples was calculated from the measured thermal diffusivity D using $\kappa_{total} = DdC_p$, where d is the geometric density and C_p is the Dulong Petit heat capacity. In Zn-containing samples, κ_{total} is higher than in the Mn end-member due to the dominance of the electronic contribution. The lattice component (κ_L) of the thermal conductivity was obtained by subtracting the electronic component (κ_{el}), calculated *via* the Wiedemann–Flanz law from the total thermal conductivity ($\kappa_{el} = LT\sigma$, where L and σ are the Lorenz number and electrical conductivity, respectively). Often, L is calculated as a function of temperature using an SPB model, thus falling in between the non-degenerate and degenerate limits (1.5 and 2.4, respectively). Using an SPB model yields a lattice thermal conductivity (Fig. 5b) for $Yb_9Mn_{4.2}Sb_9$ that is near the minimum theoretical value (κ_{min}), defined by eqn (7).

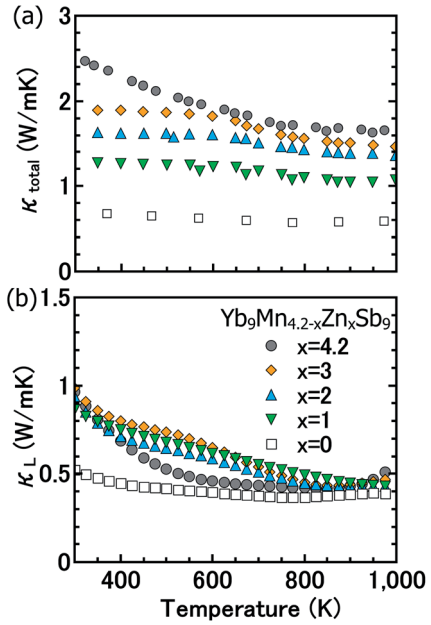

Fig. 5 (a) The total thermal conductivity of $Yb_9Mn_{4.2-x}Zn_xSb_9$ ($x = 0$, 1, 2, 3 and 4.2) increases with x. (b) The lattice thermal conductivity was estimated for Zn-containing samples using the temperature independent Lorenz numbers given in Table 3.

$$\kappa_{min} = \frac{1}{2}\left(\frac{\pi}{6}\right)^{\frac{1}{3}} k_B V^{-\frac{2}{3}}(2v_T + v_L) \quad (7)$$

here, V, v_T, and v_L are the average volume per atom, the transverse speed of sound, and longitudinal speed of sound respectively.[17,42] Room temperature ultrasonic measurements of the Zn end-member show that v_T, and v_L are comparable to the Mn analogue, as shown in Table 2, suggesting that the Zn- and Mn-based samples should have similar values of κ_L,[17] However, in the Zn-containing samples, an SPB model yields unrealistically high values of L, and thus underestimates κ_L. Thus, in Fig. 5b, rather than using an SPB model for L in the Zn-containing samples, we use L as a temperature-independent "fitting parameter" by setting $\kappa_L = \kappa_{min}$ at 923 K. The resulting values of L are given in Table 3. Note that the use of a temperature-independent L for the Zn-containing samples leads to slightly overestimated values of κ_L at lower temperatures.

Varying interstitial Zn content

Although the mobility of $Yb_9Zn_4Sb_9$ is three times higher than that of the Mn analogue, the carrier concentration is typically higher than desired for thermoelectric applications. In an attempt to control the carrier concentration by increasing the interstitial Zn concentration, we synthesized $Yb_9Zn_{4+y}Sb_9$ samples with $y = 0.2$, 0.3, 0.4 and 0.5. However, Hall measurements indicate that the carrier concentration remains constant ($n_H \sim 10^{21}$ h^+ cm^{-3}) as the amount of Zn added synthetically is varied (Fig. 6a). The Seebeck coefficients, shown in Fig. 6b, also remain nearly constant as a function of the Zn content, suggesting that the composition range of $Yb_9Zn_{4+y}Sb_9$ may be quite narrow, similar to that of the Mn analogue.

Table 2 Room temperature ultrasonic measurements: shows that the longitudinal and transverse speeds of the sound Zn compound are slightly higher than the Mn analogue

Speed of Sound	Longitudinal	Transverse
$Yb_9Zn_{4.2}Sb_9$	3228 m s^{-1}	1920 m s^{-1}
$Yb_9Mn_{4.2}Sb_9$	3070 m s^{-1}	1730 m s^{-1}

Table 3 Lorenz numbers were obtained by setting the minimum experimental lattice thermal conductivities to the calculated theoretical minimum. For the pure Mn sample, L was calculated using an SPB model as shown in ref. 13

Composition	Lorenz number ($\times 10^{-8}$ W Ω K^{-2})
$x = 1$	1.77
$x = 2$	1.61
$x = 3$	1.70
$x = 4.2$	1.50

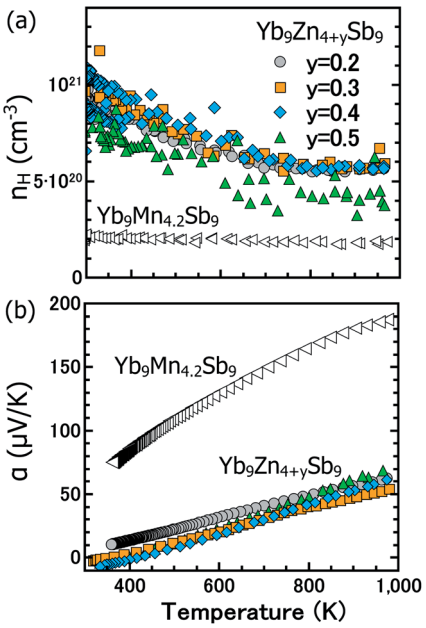

Fig. 6 (a) The carrier concentration remains unchanged in samples with synthetic compositions of $Yb_9Zn_{4+y}Sb_9$ ($y = 2$, 3, 4 and 5). (b) The Seebeck coefficients are also unaffected by varying the synthetic Zn content.

Figure of Merit

Fig. 7 shows the experimental zT of $Yb_9Mn_{4.2-x}Zn_xSb_9$ solid solution samples ($x = 0$, 1, 2, 3, 4.2) as a function of carrier concentration at 975 K. An SPB model was used to predict the figure of merit as a function of n for the $Yb_9Mn_{4.2}Sb_9$ and $Yb_9Zn_{4.2}Sb_9$ end-members (shown as dashed curves) using the parameters in Table 4. The lower effective mass and higher mobility in the Zn analogue shift the optimal carrier

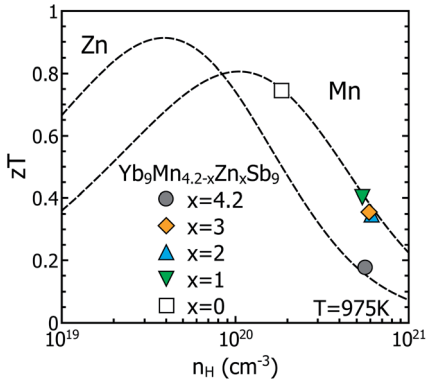

Fig. 7 The figure of merit of $Yb_9Mn_{4.2-x}Zn_xSb_9$ samples decreases with increasing carrier concentration and Zn content. The An SPB model predicts an optimized zT of 0.9 in the Zn system at $n_H = 4 \times 10^{19}$ h^+ cm^{-3}.

Table 4 The parameters for the SPB model at 975 K

	$Yb_9Zn_{4.2}Sb_9$	$Yb_9Mn_{4.2}Sb_9$
Effective mass, m^*	0.65 m_e	1.2 m_e
Intrinsic mobility, μ_0	18.65 cm^2 V^{-1} s^{-1}	5.71 cm^2 V^{-1} s^{-1}
Weighted mobility, $\mu_0 (m^*/m_e)^{3/2}$	9.77 cm^2 V^{-1} s^{-1}	7.51 cm^2 V^{-1} s^{-1}
Lattice thermal conductivity, κ_L	0.43 W mK^{-1}	0.39 W mK^{-1}
Quality factor, B	0.387	0.328

concentration downwards relative to $Yb_9Mn_{4.2}Sb_9$. The predicted maximum figure of merit is somewhat higher for the Zn analogue due to its higher weighted mobility $(\mu_0(m^*/m_e)^{3/2})$ and dimensionless quality factor[43,44] $\left(B = \left(\frac{k_B}{e}\right)^2 \frac{2e(k_BT)^{3/2}}{(2\pi)^{3/2}\hbar^3} \frac{\mu_0(m^*/m_e)^{3/2}}{\kappa_L} T\right)$, where μ_0 is an intrinsic mobility calculated by the following equation when charge carriers are scattered by acoustic phonons: $\mu_H = \mu_0 \frac{F_{-1/2}(\eta)}{2F_0(\eta)}$). However, the experimental zT of Zn containing samples is far lower than that of the Mn end-member, due to their high carrier concentrations. While the carrier concentration of $Yb_9Mn_{4.2}Sb_9$ is very close to the optimal value, samples with Zn have carrier concentrations that are far too large. However, the possibility of reducing the carrier concentration of Zn-containing samples by doping with an n-type dopant,[16,18] higher zT than that of the Mn analogue could potentially be realized in future work.

Conclusion

The Zintl compound $Yb_9Mn_{4.2}Sb_9$ is a promising thermoelectric material due to its low, glasslike lattice thermal conductivity, which is essential for high zT. In this research, the effect of substituting Zn on the Mn site in $Yb_9Mn_{4.2-x}Zn_xSb_9$ was investigated. Pursuing this strategy led to reduction by a factor of two in the valence band mass, and thus increased carrier mobility and decreased Seebeck coefficient. The thermoelectric quality factor of the $Yb_9Mn_{4.2-x}Zn_xSb_9$ system was found to be somewhat higher in the Zn analogue due to its improved mobility. However, the carrier concentration in Zn-containing samples was too high, and varying the synthetic Zn content did not lead to the desired carrier concentration control. In future studies, n-type dopants may be used to reduce the carrier concentration and achieve a higher figure of merit.

Experimental

$Yb_9Mn_{4.2-x}Zn_xSb_9$ ($x = 0$, 1, 2, 3 and 4.2) and $Yb_9Zn_{4+y}Sb_9$ ($y = 2$, 3, 4 and 5) samples were prepared by ball milling followed by hot pressing. The elements were loaded into stainless-steel vials with stainless-steel balls inside the glove box filled with argon. The materials were dry ball-milled for an hour using a SPEX Sample Prep 8000 Series mixer/mill. The fine powder was hot-pressed in high-density graphite dies using a pressure of 40 MPa on a 12 mm diameter surface. Samples were hot pressed using a maximum temperature of 1073 K for 2 hours under flowing argon, followed by 2 hours of cooling. To determine the phase purity of the products, X-ray diffraction was performed after polishing with a Philips X'Pert MPD diffractometer operating at 45 kV and 40 mA, and Rietveld analysis was performed using Philips X'part plus software. A Zeiss 1550 VP scanning electron microscope was also used to investigate the phase purity.

For measuring the thermoelectric properties, a Netzsch LFA 457 was used. Electronic resistivity and Hall coefficient were determined using the 4-point probe Van der Pauw technique with a 0.8 T field under high vacuum.[45] The Seebeck coefficient was also measured using a light-pipe method with tungsten–niobium thermocouples under high vacuum.[46]

Acknowledgements

This work was supported by the NASA Science Mission Directorate's Radioisotope Power Systems Technology Advancement Program and Japan Student Service Organization. Y. T. acknowledges support from the Sumitomo Foundation (grant no. 120567) and the Murata Science Foundation.

References

1 L. E. Bell, *Science*, 2008, **321**, 1457.
2 G. J. Snyder and E. S. Toberer, *Nat. Mater.*, 2008, **7**, 105–114.
3 E. S. Toberer, A. F. May and G. J. Snyder, *Chem. Mater.*, 2010, **22**, 624–634.
4 M. Mills, R. Lam, M. J. Ferguson, L. Deakin and A. Mar, *Coord. Chem. Rev.*, 2002, **233–234**, 207–222.
5 S. M. Kauzlarich, S. R. Brown and G. J. Snyder, *Dalton Trans.*, 2007, 2099–2107.
6 S. M. Kauzlarich, *Chemistry, Structure, and Bonding of Zintl Phases and Ions*, Wiley-VCH, 1996.
7 S. Brown, E. S. Toberer, T. Ikeda, C. A. Cox, F. Gascoin, S. Kauzlarich and G. Snyder, *Chem. Mater.*, 2008, **20**, 3412.
8 A. Zevalkink, E. S. Toberer, W. G. Zeier, E. Flage-Larsen and G. J. Snyder, *Energy Environ. Sci.*, 2011, **4**, 510.

9 W. G. Zeier, A. Zevalkink, E. Schechtel, W. Tremel and G. J. Snyder, *J. Mater. Chem.*, 2012, **22**, 9826.
10 E. S. Toberer, A. Zevalkink, N. Crisosto and G. J. Snyder, *Adv. Funct. Mater.*, 2010, **20**, 4375–4380.
11 A. Zevalkink, G. S. Pomrehn, S. Johnson, J. Swallow, Z. M. Gibbs and G. J. Snyder, *Chem. Mater.*, 2012, **24**, 2091–2098.
12 F. Gascoin, S. Ottensmann, D. Stark, M. S. Haile and G. Snyder, *Adv. Funct. Mater.*, 2005, **15**, 1860–1864.
13 C. Yu, T. J. Zhu, S. N. Zhang, X. B. Zhao, J. He, Z. Su and T. M. Tritt, *J. Appl. Phys.*, 2008, **104**, 013705.
14 A. F. May, M. A. McGuire, J. Ma, O. Delaire, A. Huq and R. Custelcean, *J. Appl. Phys.*, 2012, **111**, 033708.
15 K. Guo, Q.-G. Cao, X.-J. Feng, M.-B. Tang, H.-H. Chen, X. Guo, L. Chen, Y. Grin and J.-T. Zhao, *Eur. J. Inorg. Chem.*, 2011, 4043–4048.
16 E. S. Toberer, S. R. Brown, T. Ikeda, S. M. Kauzlarich and G. Jeffrey Snyder, *Appl. Phys. Lett.*, 2008, **93**, 062110.
17 S. K. Bux, A. Zevalkink, O. Janka, D. Uhl, S. Kauzlarich, J. G. Snyder and J.-P. Fleurial, *J. Mater. Chem. A*, 2014, **2**, 215–220.
18 E. S. Toberer, C. A. Cox, S. R. Brown, T. Ikeda, A. F. May, S. M. Kauzlarich and G. J. Snyder, *Adv. Funct. Mater.*, 2008, **18**, 2795–2800.
19 X.-J. Wang, M.-B. Tang, H.-H. Chen, X.-X. Yang, J.-T. Zhao, U. Burkhardt and Y. Grin, *Appl. Phys. Lett.*, 2009, **94**, 092106.
20 S. Brown, S. Kauzlarich, F. Gascoin and G. J. Snyder, *Chem. Mater.*, 2006, **18**, 1873–1877.
21 M. Christensen, A. B. Abrahamsen, N. B. Christensen, F. Juranyi, N. H. Andersen, K. Lefmann, J. Andreasson, C. R. Bahl and B. B. Iversen, *Nat. Mater.*, 2008, **7**, 811–815.
22 A. M. Guloy, R. Ramlau, Z. Tang, W. Schnelle, M. Baitinger and Y. Grin, *Nature*, 2006, **443**, 320–323.
23 I. Bednar, E. Royanian, S. Bühler-Paschen, E. Bauer, N. Nasir, A. Grytsiv, N. Melnychenko-Koblyuk and P. Rogl, *J. Electron. Mater.*, 2010, **39**, 1687–1691.
24 T. Yi, C. A. Cox, E. S. Toberer, G. J. Snyder and S. M. Kauzlarich, *Chem. Mater.*, 2010, **22**, 935–941.
25 H. Hua, A. Zevalkink, Z. M. Gibbs, G. J. Snyder and S. Bobev, *Chem. Mater.*, 2012, **24**, 3596.
26 G. Nolas, G. A. Slack, D. Morelli, T. M. Tritt and A. C. Ehrlich, *J. Appl. Phys.*, 1996, **79**, 4002–4008.
27 H. Kleinke, *Chem. Mater.*, 2010, **22**, 604–611.
28 X. Shi, Y. Pei, G. J. Snyder and L. Chen, *Energy Environ. Sci.*, 2011, **4**, 4086.
29 S. R. Brown, S. M. Kauzlarich, F. Gascoin and G. Jeffrey Snyder, *J. Solid State Chem.*, 2007, **180**, 1414–1420.
30 Y. Wu, A. P. Litvinchuk, E. S. Toberer, G. J. Snyder, N. Newman, A. Fischer, E. W. Scheidt, W. Scherer and U. Häussermann, *J. Appl. Phys.*, 2012, **111**, 123712.
31 A. Zevalkink, J. Swallow and G. J. Snyder, *J. Electron. Mater.*, 2012, **41**, 813–818.
32 A. Zevalkink, W. G. Zeier, G. Pomrehn, E. Schechtel, W. Tremel and G. J. Snyder, *Energy Environ. Sci.*, 2012, **5**, 9121.
33 E. S. Toberer, P. Rauwel, S. Gariel, J. Taftø and G. Jeffrey Snyder, *J. Mater. Chem.*, 2010, **20**, 9877.
34 A. May, J.-P. Fleurial and G. Snyder, *Phys. Rev. B: Condens. Matter Mater. Phys.*, 2008, **78**, 125205.
35 E. S. Toberer, A. F. May, B. C. Melot, E. Flage-Larsen and G. J. Snyder, *Dalton Trans.*, 2010, **39**, 1046–1054.
36 A. Prokofiev, A. Sidorenko, K. Hradil, M. Ikeda, R. Svagera, M. Waas, H. Winkler, K. Neumaier and S. Paschen, *Nat. Mater.*, 2013, **12**, 1096–1101.
37 S.-Q. Xia and S. Bobev, *Chem. Mater.*, 2009, **22**, 840–850.
38 S. Bobev, J. D. Thompson, J. L. Sarrao, M. M. Olmstead, H. Hope and S. M. Kauzlarich, *Inorg. Chem.*, 2004, **43**, 5044–5052.
39 G. C. E. Brechtel and H. Schäfer, *Z. Naturforsch., B: Anorg. Chem., Org. Chem.*, 1979, **34**, 1229.
40 H. Wang, A. D. LaLonde, Y. Pei and G. J. Snyder, *Adv. Funct. Mater.*, 2013, **23**, 1586–1596.
41 M. Lundstorm, *Fundamentals of carrier transport 2nd edition*, 2000.
42 D. G. Cahill and R. Pohl, *Ann. Rev. Mater. Sci*, 1988, **39**, 93–121.
43 H. Wang, Y. Pei, A. D. LaLonde and G. J. Snyder, in *Thermoelectric Nanomaterials*, eds. K. Koumoto and T. Mori, Springer, 2013, pp. 3–32.
44 Y. Pei, H. Wang and G. J. Snyder, *Adv. Mater.*, 2012, **24**, 6125–6135.
45 K. A. Borup, E. S. Toberer, L. D. Zoltan, G. Nakatsukasa, M. Errico, J. P. Fleurial, B. B. Iversen and G. J. Snyder, *Rev. Sci. Instrum.*, 2012, **83**, 123902.
46 C. Wood, D. Zoltan and G. Stapfer, *Rev. Sci. Instrum.*, 1985, **56**, 719.